Coma pattern-based autofocusing unlocks superior performance in unravelling single-cell dynamics during bacterial cold shock response

SIHONG LI[1,4], ZHIXIN MA[1,2,4], YUE YU[1,4], JINJUAN WANG[1], YAXIN SHEN[1], XIAODONG CUI[3], XIONGFEI FU[1,2], AND SHUQIANG HUANG[1,2*]

[1]Key Laboratory for Quantitative Synthetic Biology, Shenzhen Institute of Synthetic Biology, Shenzhen Institutes of Advanced Technology, Chinese Academy of Sciences, Shenzhen, 518055, China

[2]University of Chinese Academy of Sciences, Beijing, 100049, China

[3]Department of Physics, The University of Hong Kong, Hong Kong

[4]These authors contributed equally: Sihong LI, Zhixin MA, Yue YU.

*Corresponding authors: Shuqiang HUANG, shuqiang.huang@siat.ac.cn

Abstract

Cutting-edge studies in live cell dynamics place increasing demands on microscopy imaging, and focus stability during acquisition is a critical factor in obtaining high-quality image data. Current autofocusing solutions are limited to focusing precision and range, thus impeding their application in high-accuracy research. Here, we introduce LUNA (locking under nanoscale accuracy), an innovative autofocusing method that leverages the coma pattern of detection light to characterize focus drift. LUNA improves the focusing precision down to 3 nm and extends the focusing range to at least 40 times the objective depth-of-focus. These advancements enable us to investigate how bacteria adapt to temperature change at the single-cell level, revealing a series of novel insights into bacterial cold shock response mechanisms. This approach addresses the complexities of growth dynamics, growth mode transition, division synchronization, and size regulation during the adaptation period, which present significant challenges for traditional analytical methods. Notably, the controversies between the growth lag of batch culture and continuous growth at the single-cell level are successfully explained based on scattering theory. LUNA shows enhanced performance in improving existing advanced microscopy technologies and demonstrates excellent potential for expanding state-of-the-art research in biology.

27 ***Main text***

28 Microorganisms in their natural environments may face sporadic or recurrent challenges due to abrupt
29 temperature fluctuations, driving the evolution of various adaptive strategies. These microbial responses
30 are strongly connected to anthropogenic climate change. Quantitative understanding of such adaptations
31 remains challenging[1] and may immensely contribute to effective mitigation of future ecology[2]. A typical
32 complicated process upon temperature drop, known as cold shock response (CSR), has yet to be fully
33 elucidated for microorganisms such as bacteria[3]. Routine studies of CSR count on batch culture, which
34 may limit our understanding due to the inability to uncover the physiological dynamics of individuals
35 masked by averaged data. To understand how CSR incorporates into the system-wide picture, equipping
36 large-scale spatiotemporal microscopy imaging with single-cell level resolution is important. Single-cell
37 investigations that rely on microscopy images offer opportunities for unbiased quantitative analysis of CSR,
38 yet are rarely reported. Microscopy studies typically involve capturing multiple fields of view over hours
39 to days to collect image data, making it crucial for the samples to remain focused[4]. The inevitable and
40 unpredictable focus drift that may originate from environmental perturbations, such as the drastic
41 temperature drop for CSR, necessitates an autofocus system to compensate. A variety of strategies have
42 been developed to this end over the years[5-12] (Supplementary Note 1). Nevertheless, limited focusing
43 precision and range make it difficult for current solutions to cope with stringent requirements of biological
44 research, for instance, imaging across large volume[7], single-molecule localization[13] or super-resolution
45 imaging[9], large span temperature shift[14], etc.

46 Herein we propose LUNA (locking under nanoscale accuracy), a novel reflection-based autofocusing
47 method that breaks through the limitations of the current solutions. LUNA is demonstrated to achieve
48 exceptional focusing precision down to 3 nm while offering an ultra-large focusing range of at least 40
49 times the depth-of-focus (DOF) of the objective. With the help of LUNA, we investigated the physiological
50 response of bacterial CSR at the single-cell level by continuously monitoring thousands of individual
51 *Escherichia coli* cells for more than ten hours. Bacteria enter a lag period (acclimation) immediately after

52 cold shock, widely considered a growth arrest, as it is manifested by a constant optical density (OD)[15,16].
53 However, we discovered that, on the contrary, *E. coli* cells continued to proliferate during the acclimation.
54 Our research revealed significant insights into mitigating growth deceleration and facilitating growth mode
55 transition, and further found that they resonate closely with prior molecular-level studies. Remarkably,
56 distinct cells exhibit synchronized growth dynamics in timing and cycle number. Concurrently, these cells
57 tend to employ their size regulation strategies to adapt. Furthermore, we analyzed our batch culture results
58 on the basis of scattering theory, and concluded that the OD lag is actually the outcome of the synergy of
59 changes in bacterial concentration and volume, which explains the controversies between single-cell and
60 population observations.

61 **Results**

62 **LUNA optical principle**

63 In conventional reflection-based autofocusing methods, when an objective focuses the focus-aid light
64 beam at the reflection interface, the intensity and contrast of the light spot are the highest. But they decrease
65 rapidly as the defocus distance increases, resulting in a constrained focusing range. Typically, it is also
66 necessary to compensate for the offset distance between the desired focal plane and the reflection interface.
67 However, the additional movement for the compensation leads to more fluctuations that could reduce the
68 focusing accuracy[17]. To alleviate these limitations, we introduce coma aberration in the diffraction pattern
69 of the reflected auxiliary laser beam. This allows LUNA to lock onto the focal plan directly rather than
70 introducing the offset, substantially improving focusing accuracy and range.

71 We investigated a thorough optical model for the propagation of an off-axis laser beam through an
72 ideal lens in the presence of coma aberration (Methods, Supplementary Note 2). This model gives an
73 analytical expression of light distribution near the focus based on diffraction theory (Fig. 1a). According
74 to the Huygens-Fresnel principle, the light disturbance at an arbitrary observation point P in the vicinity of
75 the focal point is determined by summing the contribution of each point Q located where the incident
76 Gaussian beam intersects the reference sphere on the pupil plane[18]. The presence of coma aberration causes

the intensity distribution of the laser spot to concentrate on one side, forming a high-contrast crescent diffraction pattern (Fig. 1b). The centroid locations (center of mass) of the brightest pattern along the z-axis exhibit a monotonic trend over a wide range away from the focal point (Fig. 1c), suggesting that the defocus distance can be directly determined by the relative lateral displacement of the centroid location, which can be precisely measured. The contrast of the laser spot away from the focal plane is significantly enhanced compared to aberration-free system with the Airy pattern, thereby improving the accuracy of defocus detection and the focusing range (Fig. 1d).

This model serves as a guide for the design and implementation of LUNA, which was deployed in a bespoke infinity-corrected microscope system for spatiotemporal imaging (Methods, Extended Data Fig. 1a). To validate and optimize the performance of LUNA, a numerical simulation of the optical setup was carried out based on ray tracing (Fig. 1e, Extended Data Fig. 1b-d). The line projection of the crescent spot in the implementation conforms well with the simulation and shows supreme contrast. The simulation shows that LUNA has sufficient sensitivity (Fig. 1f, the defocus distance Δz can be magnified about 23 times at the detection plane). LUNA allows users to set the focal plane of interest by defining the centroid location on the detector as the origin without the need of any offset distance (Fig. 1g, Extended Data Fig. 1e). This fundamentally decreases the intrinsic motive noises. Additionally, the wide focusing range allows a large tolerance for the offset. In the event of focus drift, an autofocusing procedure is initiated by repositioning the line spot to the origin through a feedback control.

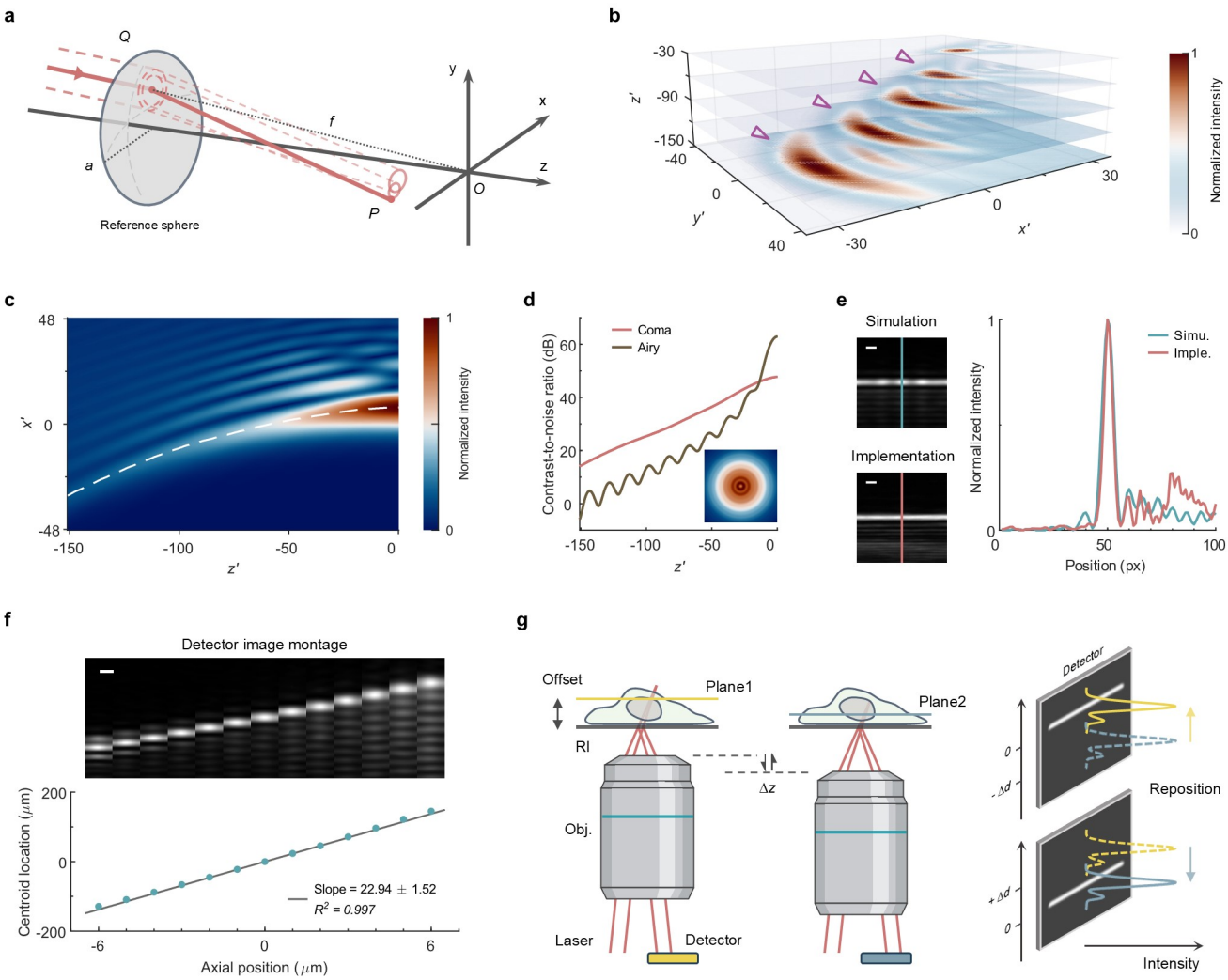

Fig. 1 | Illustration of optical principle. a, Schematic diagram of the optical model. An off-axis Gaussian beam (red lines) propagates through an objective lens of radius *a* and focal length *f*. *Q*, point in which a light ray in the image space intersects the Gaussian reference sphere; *P*, arbitrary point near focus. **b**, Computed intensity distribution in the dimensionless space under 100× objective. Coordinates (x', y', z') equals ($k\beta x$, $k\beta y$, $k\beta^2 z$), where k is wavenumber, $\beta = a / f$. Images at each axial position were individually normalized. Triangle markers indicate the crescent spots. **c**, Computed intensity distribution in x-z space. The dashed line indicates the centroid locations of the brightest crescent spots along the z-axis. Image contrast was adjusted for better exhibition (Gamma = 0.5). **d**, Comparison of spot contrast with and without coma aberration. Inset image: Airy pattern at -90 axial position in the dimensionless space in an aberration-free system. **e**, Comparison of numerical simulation and implementation. Left panel: Retrieved images

from the detection planes in the simulation and implementation, respectively. Right panel: intensity profiles along the lines in both images. px, pixel. **f**, Magnified defocus distance on the detection plane in the simulation. Linear regression with slope (95% confidence intervals) and fit goodness is shown. Scale bars in **e** and **f**, 60 μm. **g**, Working principle of LUNA. Set Plane1 (Plane2) as the interested focal plane by specifying the centroid location of the line spot on the detector as the origin. The defocus distance Δz between the target and defocused Plane2 (Plane1) is inferred by the displacement Δd. Autofocusing is then achieved by repositioning the spot to the origin. RI, reflection interface; Obj., objective.

Performance analysis of LUNA

The relationship between the measured centroid location and the physical axial position was calibrated (Methods, Fig. 2a, Extended Data Fig. 2a). LUNA shows an extensive focusing range and good linearity in a particular range (termed as linear range) around the focus, considerably exceeding the corresponding objective DOF. Within the linear range, the lateral displacement Δd of the laser spot centroid is given by

$$\Delta d = A_M \cdot \Delta z \tag{1}$$

where A_M represents the magnification coefficient. Despite some bias, this relationship can still be used to roughly estimate Δz outside the linear range. The measurement repeatability was used to evaluate the degree of consistency during multiple tests. The results highlight the excellent ability of LUNA to accommodate large defocus distances (Extended Data Table 1), thereby facilitating precise focusing across diverse spatial scales.

A drift threshold value was preset as a constraint criterion to determine the defocus status. LUNA effectively maintains the focal plane within a tight margin, while without compensation the focus drift can escalate to several microns within a dozen minutes (Fig. 2b). Our results demonstrate that the focusing accuracy and precision (mean and standard deviation used)[19] remain small and consistent across different thresholds and objectives (Fig. 2c, Extended Data Fig. 2b). Since the nature of the feedback procedure results in an almost uniform distribution of errors, the precision is determined by the threshold (≈ theoretical value, threshold / √3). The best achievable precision is approximately 3 nm in our configuration (Extended

Data Table 1). Apart from the centroid displacement caused by focus drift, other perturbations affecting the precise localization of the centroid primarily arise from temporal fluctuations of the spot intensity. Numerical simulations were conducted to evaluate the effect of perturbations on the centroid location, which is limited to a few nanometers and can be ignored (Methods, Fig. 2d, Extended Data Fig. 2d). Due to the small variance in focusing accuracy, the drift followed the previous autofocusing procedure is slight (Fig. 2e). This indicates that LUNA is suitable for common live or time-lapse imaging.

Short focusing time is another crucial feature of an autofocus system, especially for fast image acquisition. The focusing time was statistically tested under different procedure onset frequencies (Fig. 2f, Extended Data Fig. 2e). At lower frequencies, the focusing time exhibits a relatively significant variation across different thresholds. This variation can be attributed to an increase in the number of feedbacks needed to stabilize the focus, which arises from the larger axial drift presented. In practical applications, there is a tradeoff between pursuing better precision and shorter time consumption when determining the optimal threshold. Setting a sufficiently large threshold (i.e., greater than 15 nm, which is the optimal value in this work) and a frequency above 10 Hz result in no considerable difference in focusing time under different conditions.

These advantages equip us to cope with drastic environmental perturbations during imaging, thereby facilitating the application of LUNA-based microscopy in some cutting-edge biological research. Herein, we adopt LUNA to get a deeper understanding of bacterial CSR. Cold shock (CS) is usually executed by cooling the bacterial culture medium from 37 ℃ to below 15 ℃ in a few minutes. The physiological dynamics of bacterial cells during CS, one of the vital CSR parameters, has never been observed microscopically due to the limited competence of the current techniques to tackle severe axial drift. To exert CS rapidly and uniformly on each cell, we integrated a microfluidic-based temperature control device into the bespoke microscope (Methods, Extended Data Fig. 3a). The microfluidic chip can trap single cells in separate microchannels and maintain steady growth[20], immersed in circulating water for temperature maintenance and change. Relative drift between consecutive timepoints in our time-lapse imaging (37 ℃

to 14 °C within 5 minutes) can reach a maximum of ~10 μm, much larger than the DOF (Fig. 2g, Extended Data Fig. 3b). LUNA can compensate for the significant drift, keeping the high-throughput imaging in focus (~1,100 cells simultaneously) (Fig. 2h, Supplementary Video 1). The average focusing time at each location is around 0.6 seconds, enabling high temporal resolution imaging.

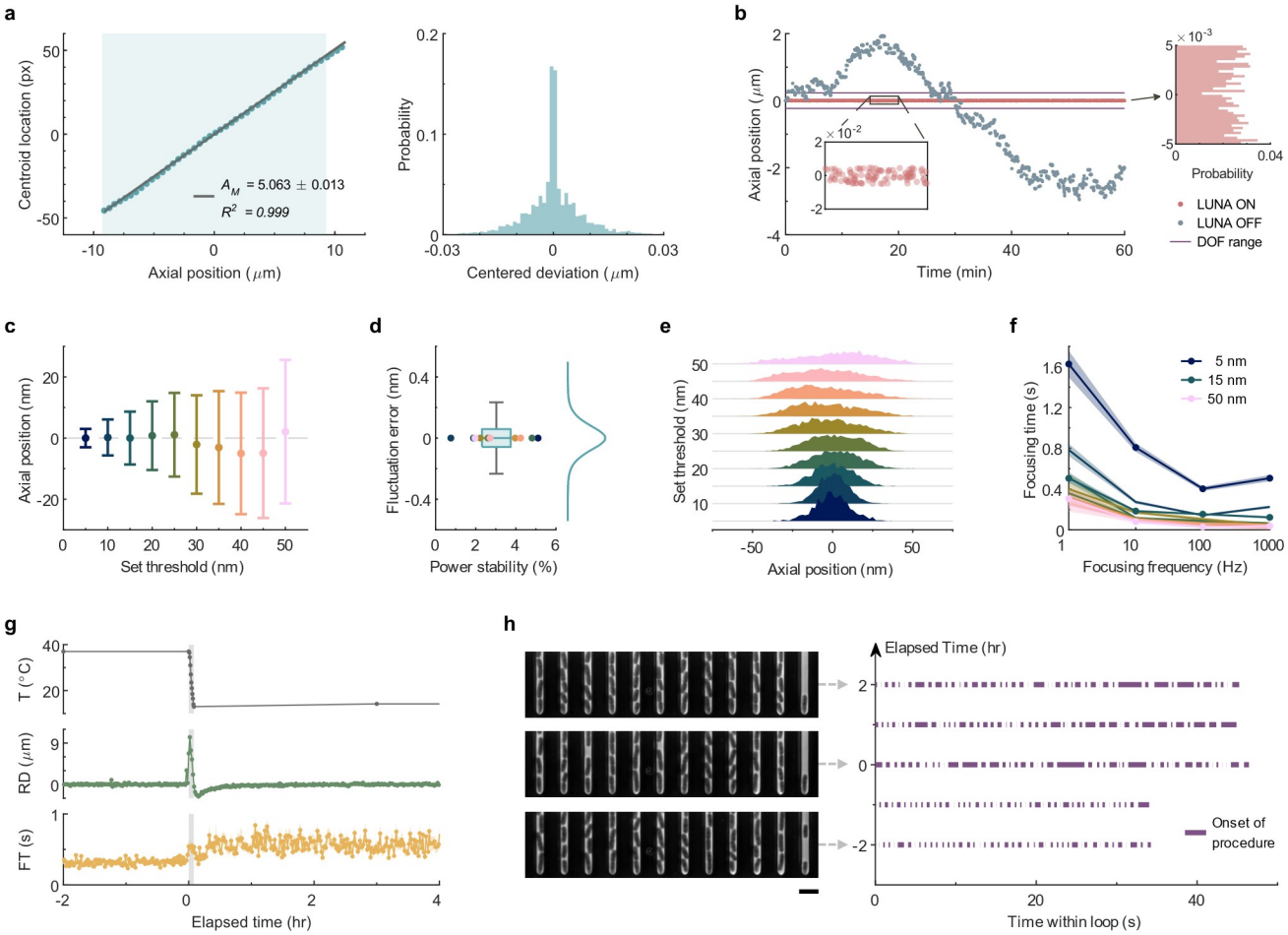

Fig. 2 | Comprehensive performance metrics of LUNA. a, Calibration curve (left) and measurement error distribution (right). Shaded region in the left panel indicates the linear range. Linear regression with slope (95% confidence intervals) and fit goodness is shown. **b**, Focus drift monitoring at 1 Hz in the laboratory environment. Right histogram shows the focal plane positions after each autofocusing procedure. **c**, Focusing accuracy and precision assessment. Dots and error bars represent the mean and s.d. values of the focus errors. Color palette in **c-f**, different set thresholds. **d**, Impacts of intensity fluctuations on focusing accuracy. All data for the 10 thresholds are presented as box plot with the edges at the 0.25 and 0.75

quantiles, the central line at the median, and the whiskers at the minima and maxima within 1.5× interquartile range from the box. Dots indicate average power stability of the 10 thresholds. Colored line, probability distribution. **e**, Ridgeline plot of relative drift after the previous autofocusing procedure. **f**, Focusing time measurement for autofocusing procedures at different intervals. Lines those marked with dots emphasize the representative constraints. **g**, System states over time when imaging bacteria. CS occurs at $t = 0$. T, temperature of cell environment; RD, relative drift of sample stage before autofocusing; FT, corresponding focusing time. Data in scatter form represent the average of all imaged sites ($n = 45$). Shaded region indicates the rapid temperature drop period. Error bands in **f**, **g**, s.e.m. **h**, Representative images and onset of autofocusing procedure. Scale bar, 4 μm. Intervals between consecutive procedures indicate the time consumption of phase-contrast imaging and stage motion.

Time-resolved regulation of growth without arrest under CS

LUNA enables us to investigate the time-resolved behavior of bacterial CSR at the single-cell level. Cell morphological dynamics were extracted from time-lapse image sequences through a self-developed identification algorithm for subsequent statistical analysis (Methods, Supplementary Note 3). Single cells located at the bottom of each microchannel are inherited from one generation to the next after each cell division (Fig. 3a). We distinguish the bacterial generations: the one encountering CS (G0), those before CS (GN), and those after CS (G1, G2, etc.). Upon application of CS, sustained division events are still maintained throughout the acclimation (~2 hours in our batch culture), rather than stopping growth as generally believed. Notations in the following analysis are presented in Fig. 3b. To investigate sub-cell-cycle responses in detail, we grouped cell lineages by the relative CS onset time since cell birth of G0 (ξ).

We classified the acclimation into three phases based on the growth rate (λ) characteristics (Fig. 3c, d). Phase I involves the cooling process from 37 °C to 20 °C (to ~3 min), with an average growth deceleration ($d\lambda / dt$) of approximately -6.25 hr^{-2}. Surprisingly, the temperature dependence of λ during this dynamic process also follows Arrhenius law (Extended Data Fig. 4a), just as it does at the population level in steady-state[1]. The growth deceleration in Phase II (to ~10 min, approximately -2.97 hr^{-2} on average) is

192 immediately mitigated. This is reminiscent of the sustained elongation of already initiated protein synthesis
193 before CS[21,22] and the probable rapid response to temperature changes of constitutively expressed cold
194 shock proteins (CSPs, such as CspE and CsdA) at 37 °C[23,24]. These CSPs are generally considered to restore
195 essential biochemical reactions during the acclimation, especially translation initiation[25]. Phase III
196 continues until the end of the acclimation (to ~120 min), during which the temperature is kept constant at
197 14 °C. The further mitigated deceleration (approximately -0.18 hr^{-2} on average) may be explained by the
198 combined effects of newly synthesized CSPs and ribosome regulation. After CS, cells halt the synthesis of
199 new ribosomes and allocate resources to produce more CSPs[15,26]. Even with the continuous dilution of
200 ribosomes as cells grow, the upregulated CSPs promote the subsequent restoration of cellular physiological
201 activities (Extended Data Fig. 4b). Later in the acclimation, ribosome synthesis gradually recovers, and
202 CSPs are downregulated due to the reallocation of limited resources. We speculate that the ribosome
203 concentration in each cell decreases monotonously during this process, leading to a continuously decreasing
204 λ and eventually establishing a new homeostasis of λ inherited by the offspring after acclimation (Fig. 3c).

205 The impact of CS on ribosome allocation might also explain the transition in growth modes from
206 exponential to linear growth immediately and eventually back to exponential growth in late phase III (Fig.
207 3e, Extended Data Fig. 4c-f). *E. coli* cells can sustain exponential growth during steady-state[27], which is
208 based on the view of "autocatalytic loop" of biomass synthesis[28]. This means that a fixed portion of total
209 synthesized proteins is allocated to the ribosomes[29]. The pause of new ribosome synthesis after CS prevents
210 the "autocatalytic loop", thereby resulting in linear growth. Meanwhile, upregulated expressions of
211 ribosome assembly regulatory factor RbfA and translation initiation factors maintain the turnover of
212 existing ribosomes[30,31], which ensures minimal growth. As the synthesis recovers, a new homeostasis of
213 "autocatalytic loop" in biomass synthesis is achieved, i.e., the cell completes cold adaptation and resumes
214 exponential growth.

215 Further studies on cells with distinct ξ and their progeny after CS revealed that cells exhibit highly
216 consistent CSR. The changes in λ are fully synchronized in time, with the exact time lag between any pair

of ξ not exceeding 2 min (Fig. 3c, Extended Data Fig. 5a). This is reasonable for the existence of constitutively expressed CSPs under steady-state. Surprisingly, the exact number of elapsed cycles at any moment since the CS event is also consistent across different cells (Fig. 3f, g, Extended Data Fig. 5b, c). We verified the consistency of the elapsed cycle deviation over time. Compared with the steady-state, the deviation after CS does not increase significantly and is still within a small range. In other words, cells encountering a relatively late CSR will "accelerate" divisions to maintain synchronization.

E. coli cells can regulate their morphology in response to temperature stimuli[14]. We observed that they try to maintain sufficient size (length) increments in G0 as in the normal steady-state and then take an additional 3-4 generations for length stabilization (Fig. 3h, Extended Data Fig. 5d, e). The division length (L_d) difference between G0 and its corresponding predecessor of each cell is small (median of -1.3%). However, the earlier the CS occurs, the more likely the L_d decreases. It appears that the size regulation has a delayed onset mechanism in CSR, triggered by the completion of current division. Besides, *E. coli* cells maintain a narrowly distributed size under the steady-state. This size homeostasis mechanism can be well explained by the hypothesis that cells add a constant length extension ΔL independent of length at birth L_b between divisions (or "adder")[27,32,33]. Kendall's τ between rescaled ΔL and L_b and the linear regression were examined, showing almost no significant correlation (Fig. 3i, $|\tau| \leq 0.1$ for all generations). These data suggest that this "adder" behavior could be maintained consistently during CSR.

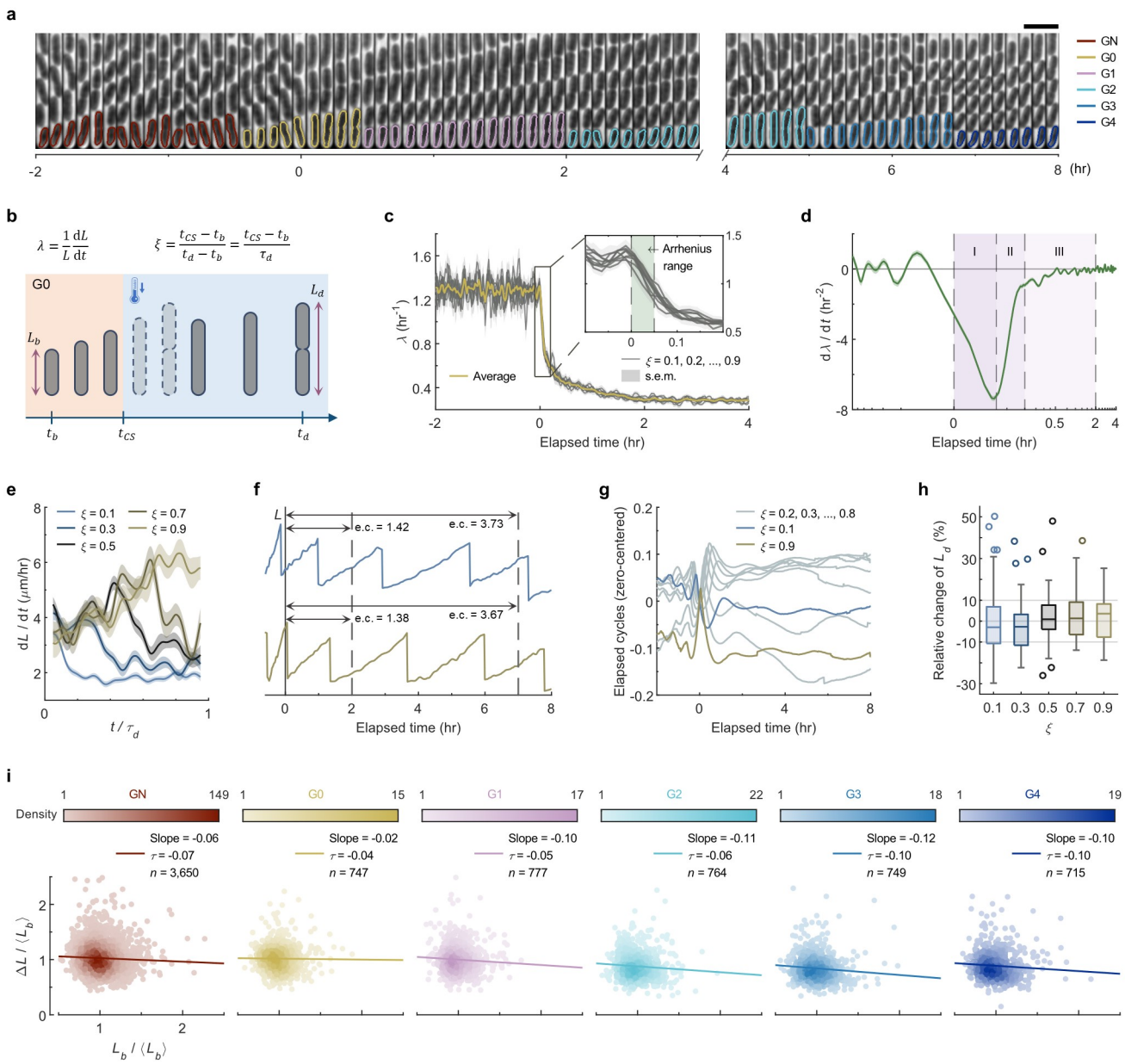

Fig. 3 | Investigation of single-cell phenotype in CSR using LUNA. a, Temporal montage of a single microchannel in the microfluidic chip. CS occurs at $t = 0$. Image was superimposed by cell contours with identified colors according to their generation marks. Timeline unit, hour. Intervals in the left and right panels are 6 and 10 mins, respectively. Scale bar, 4 μm. **b**, Notations in cell cycle. λ, growth rate; ξ, relative CS onset time since cell birth; τ_d, interdivision time. Dashed cells, expected exponential growth in the steady-state. **c**, Growth dynamics of different group of cells and average. Arrhenius range of growth is shaded in inset. **d**, Growth deceleration as function of time. The time window of the three Phases is 0-3 min, 3-10 min and 10-120 min, respectively. **e**, Elongation rate in G0 of different groups, only 5 of 9 are

shown. Cell number of each group: 137, 76, 67, 46, 38. Error bands in **c-e**, s.e.m. **f**, Representative lineages with synchronized elapsed cycles (ξ is 0.10 and 0.90, respectively). e.c., elapsed cycles. **g**, Elapsed cycle numbers that centered by the average of all lineages as functions of time. Errors shown in Extended Data Fig. 5c. **h**, Percentage change of division length between G0 and their corresponding predecessors. Grouped data are presented as box plots with the edges at the 0.25 and 0.75 quantiles, the central line at the median, and the whiskers at the minima and maxima within 1.5× interquartile range from the box. Circles, outliers outside the whiskers. **i**, Relationship between length extension and birth length across generations (rescaled by the expectation of L_b). Gradient colors indicate data density of each generation. Linear regressions of all the measured cycles and Kendall's τ are shown. n represents cycle number.

The comprehensive effect of CSR determines the acclimation of growth curve

The discoveries from single-cell experiments revealed that *E. coli* continues to proliferate after CS, prompting us to reexamine batch culture experiments (Methods). In our results, the measured OD_{600} curve indeed showed an acclimation immediately following the rapid temperature downshifting (Fig. 4a, Extended Data Fig. 6a). Nevertheless, the cell concentration (C) continued to increase at a lower rate during the acclimation. Meanwhile, the cell volume (V) decreases. Consistently with single-cell experiments, these results confirmed that bacterial divisions do not stop after CS.

Therefore, a complex question is raised: given that OD is a widely accepted indicator of total dry mass in experiments[34,35], why does the bacterium's growth continue while the OD levels off? In theory, OD value involves not only the bacterial concentration, but also light scattering by individual cells. Rayleigh scattering is the predominantly scattering of light by small particles compared to the wavelength of incident light. The Rayleigh-Gans approximation can provide more accurate results if the interference scattered from different parts of the scatterer is taken into account[36] (Methods, Supplementary Note 4). Numerical simulations were performed to compute the total scattering cross section σ of well-dispersed typical *E. coli* cells (Extended Data Fig. 6b, c). The results show that σ is not correlated to the aspect ratio (Pearson

correlation coefficient -0.07) but is theoretically proportional to $V^{1.34}$ (Fig. 4b, c). OD value is then given by $K\sigma C$, where K is constant. A concise dependency can be extracted as:

$$\mathrm{OD}_{600} = \alpha \rho_{dry}^{2} V^{1.34} C \tag{2}$$

where α is constant coefficient depending on the measurement conditions, ρ_{dry} is the cellular dry-mass density.

In the batch culture, σ could be computed from the ratio of OD to C. It has a power relationship with V, which agrees well with the theoretical relationship (Fig. 4d, Extended Data Fig. 6d). This also indicates that ρ_{dry} remains stable all the time even when cells experiencing CS[28]. Therefore, a theoretical OD curve can be deduced according to equation (2) (Fig. 4a, Extended Data Fig.6a). The relationship holds when single scattering is applicable, which corresponds to the volume concentration of scatterer is less than 0.001[37] (equivalent to $\mathrm{OD}_{600} < 0.5$ for *E. coli*). Batch culture studies without CS verified that when C is high, multiple scattering must be considered, and the cells become physiologically different, leading to increased deviations (Extended Data Fig. 7a-c)[38,39].

To further verify the validity of equation (2), total dry mass per ml ($M = \rho_{dry}VC$) as a function of measured OD is also computed. In a steady-state, M shows an excellent linear relationship with OD (Fig. 4e, Extended Data Fig. 6e, 7c). When bacterial population reaches a new steady-state at a lower temperature, the linear relationship can be well-fitted again. Some mass increment (ΔM) during the acclimation indicates population growth. In contrast, the corresponding OD may even decrease slightly due to the complicated interplay (Extended Data Fig. 7d, e). A protein quantification measurement verified that total protein during the acclimation still increased by about 13%, consistent with the trend and value of computed ΔM (Methods). Overall, these results suggest that OD is not an appropriate indicator of total dry mass under perturbed growing environment or unsteady growth, particularly for bacterial CS.

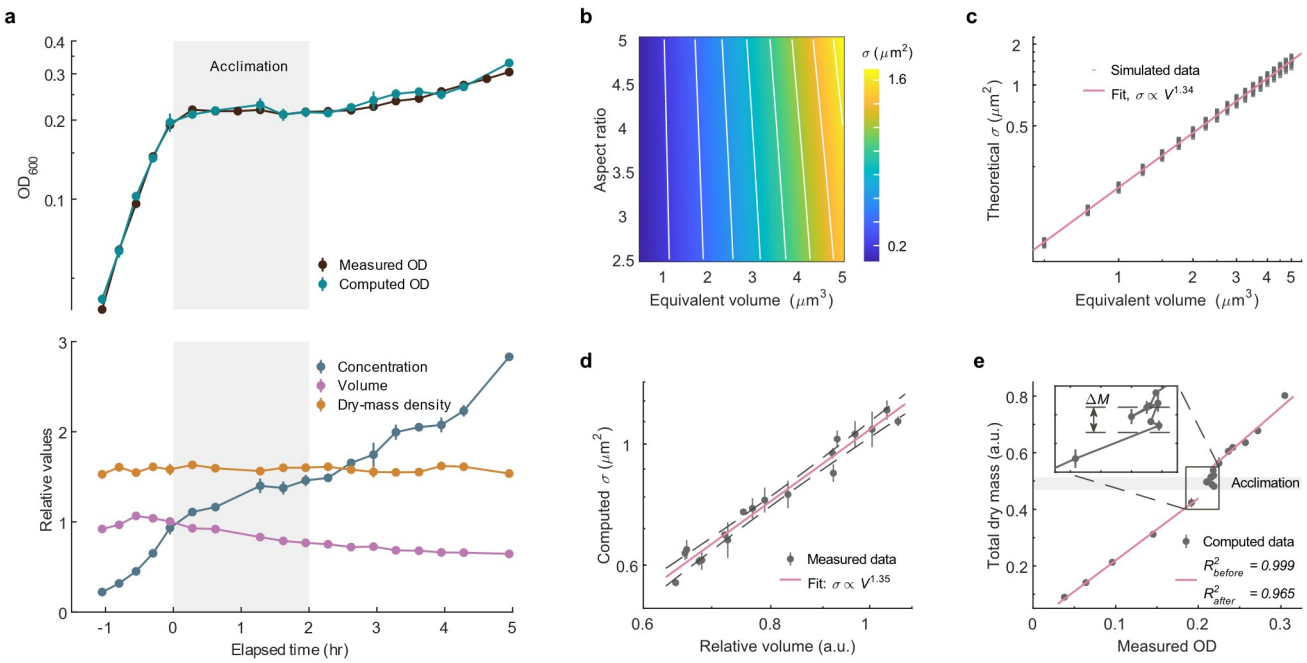

Fig. 4 | Analysis of CS experiments of batch culture. a, Measurements with temperature dropped to 14 °C. Measured and computed OD_{600} values (top). Computed data was scaled at *t0*. Bottom: cell concentrations and average volumes extracted from the flow cytometer, normalized to *t0* and average value before CS, respectively. Relative cell density was computed and scaled for present. Shaded region indicates the acclimation. **b**, Simulation of cells with varying parameters. Color bar represents computed total cross section σ for each cell. White contour lines indicate the elevation of σ. **c**, Theoretical σ across a range of equivalent cell volumes of simulated cells in **b**. Power exponent was determined by linear regression on the logarithmically transformed data (R^2 = 0.996, confidence interval is ±0.01). **d**, Computed σ from experimental data as function of relative volume. Power exponent was obtained as same process in **c** (R^2 = 0.971, confidence interval is ±0.12). Dashed lines indicate the 95% prediction bounds. a.u., arbitrary units. **e**, Computed total dry mass plotted as a function of OD, together with linear fittings. Fitting for the acclimation has a R^2 of -0.263 (Pearson correlation coefficient -0.00). Mass increment during the acclimation is indicated as the height of the shaded area and marked in the inset. Error bars in **a**, **d**, **e**, s.d.

Discussion

303 Time-lapse microscopy is the pivot for characterizing cellular dynamics, where maintaining the focus
304 precisely during environmental fluctuations remains challenging (Supplementary Video 2). Under the
305 instruction of an optical model with coma aberration, we developed LUNA with nanoscale precision and
306 ultra-large focusing range, which can lock the focus directly and rapidly. Four representative objectives
307 were tested to evaluate LUNA's comprehensive performance metrics based on a range of criteria[40,41]. In
308 our microscope, the precision is limited by the accuracy of the servo motor used, which can be improved
309 by employing piezoelectric motors with higher positioning accuracy to drive axial movement. The in-depth
310 time consumption analysis demonstrated the applicability of LUNA in tracking defocus variations either
311 in real-time or time-lapse imaging. Although the focusing time is sufficient for our experiments, it can be
312 reduced even further with faster motors and well-calibrated feedback control algorithms.

313 LUNA is successfully exploited in more extreme out-of-focus scenarios caused by severe temperature
314 fluctuations to study bacterial CSR at the single-cell level. The physiological analysis revealed many
315 characteristics of CSR that have been covered by population-level OD measurement. A three-phase growth
316 decrement phenomenon in acclimation echoes molecular-level mechanisms, especially the dynamics of
317 protein synthesis. Effects related to ribosome allocation may also explain the transition to a linear growth
318 mode. Another noteworthy finding is that CSR is reflected in single-cell growth dynamics quite quickly,
319 with the reduction in λ immediately and significantly mitigated when the temperature dropped below 20 °C,
320 which is widely regarded as a triggering threshold of CSR. This reminds us of a set of sensing and
321 responsive molecules in cells standing by to tackle sudden temperature changes that may happen at any
322 time and lead to the synchronization of CSR. In addition, our results show that OD is not an accurate growth
323 indicator in batch culture studies when the cell phenotype (size and division) is not maintained. We
324 summarized the OD value dependence and explained the paradoxical phenomenon of growth arrest
325 observed in population. Another scenario where OD may decrease occurs during nutrient downshift, in
326 which the bacteria size reduces[42].

From the perspective of evolution, it is reasonable for bacteria to keep growing and dividing after CS. Individuals who can increase the population size during the acclimation can gain a competitive advantage when entering a new steady-state. Based on the retention of some CSPs and nucleic acids at optimal growth temperatures, it is foreseeable that bacteria may have developed the ability to sustain growth after CS long time ago. Furthermore, such adaptive systems can also cope with transient and periodic temperature fluctuations, allowing cells to recover more swiftly to optimal growth following brief CS events without the need to reboot their physiological activities. To further understand the mechanisms underneath those phenomena, more physiological changes involving molecular mechanism exploration can be investigated[43,44]. Besides, there are still unresolved questions. For example, it needs to be clarified why different bacterial species have different adaptation strategies in CSR in population experiments[3]; the bacterial response remains unexplored upon temperature shifting back to optimal growth conditions. With LUNA, investigations at the single-cell level may enlighten us to explore those future issues further appropriately.

Beyond the instance in this work, LUNA offers excellent precision and can overcome the limitations of existing autofocusing solutions, thus enhancing many cutting-edge microscopy technologies, including super-resolution, single-molecule imaging, etc. Given its large focusing range, LUNA is capable of easily locking the focus in microscopy imaging across large volumes or at greater depths, such as multiphoton or light-sheet microscopy. The implementation of our method avoids complicated optics, alignment, and operation routines, posing its universal applicability to general microscopy techniques. As a result, we anticipate that LUNA will prevail in various research and industrial applications.

References

1 Knapp, B. D. & Huang, K. C. The Effects of Temperature on Cellular Physiology. *Annu. Rev. Biophys.* **51**, 499-526 (2022).

2 Cavicchioli, R. *et al.* Scientists' warning to humanity: microorganisms and climate change. *Nat. Rev. Microbiol.* **17**, 569-586 (2019).

3 Zhang, Y. & Gross, C. A. Cold Shock Response in Bacteria. *Annu. Rev. Genet.* **55**, 377-400 (2021).

4 Stephens, D. J. & Allan, V. J. Light microscopy techniques for live cell Imaging. *Science* **300**, 82-86 (2003).

5 Yazdanfar, S. *et al.* Simple and robust image-based autofocusing for digital microscopy. *Opt. Express* **16**, 8670-8677 (2008).

6 Ghaznavi, F., Evans, A., Madabhushi, A. & Feldman, M. Digital Imaging in Pathology: Whole-Slide Imaging and Beyond. *Annu. Rev. Pathol.: Pathol. Mech. Dis.* **8**, 331-359 (2013).

7 Silvestri, L. *et al.* Universal autofocus for quantitative volumetric microscopy of whole mouse brains. *Nat. Methods* **18**, 953-958 (2021).

8 Pinkard, H., Phillips, Z., Babakhani, A., Fletcher, D. A. & Waller, L. Deep learning for single-shot autofocus microscopy. *Optica* **6**, 794-797 (2019).

9 Wu, Y. C. *et al.* Three-dimensional virtual refocusing of fluorescence microscopy images using deep learning. *Nat. Methods* **16**, 1323-1331 (2019).

10 Li, S., Cui, X. & Huang, W. High resolution autofocus for spatial temporal biomedical research. *Rev. Sci. Instrum.* **84** (2013).

11 Zhang, X., Zeng, F., Li, Y. & Qiao, Y. Improvement in focusing accuracy of DNA sequencing microscope with multi-position laser differential confocal autofocus method. *Opt. Express* **26**, 895-904 (2018).

12 Bathe-Peters, M., Annibale, P. & Lohse, M. J. All-optical microscope autofocus based on an electrically tunable lens and a totally internally reflected IR laser. *Opt. Express* **26**, 2359-2368 (2018).

13 Beghin, A. *et al.* Localization-based super-resolution imaging meets high-content screening. *Nat. Methods* **14**, 1184-1190 (2017).

14 Knapp, B. D., Zhu, L. L. & Huang, K. C. SiCTeC: An inexpensive, easily assembled Peltier device for rapid temperature shifting during single-cell imaging. *PLoS Biol.* **18** (2020).

15 Zhang, Y. *et al.* A Stress Response that Monitors and Regulates mRNA Structure Is Central to Cold Shock Adaptation. *Mol. Cell* **70**, 274-286 (2018).

16 Jones, P. G., VanBogelen, R. A. & Neidhardt, F. C. Induction of proteins in response to low temperature in Escherichia coli. *J. Bacteriol.* **169**, 2092-2095 (1987).

17 Pengo, T., Munoz-Barrutia, A. & Ortiz-De-Solorzano, C. Halton sampling for autofocus. *J. Microsc.* **235**, 50-58 (2009).

18 Born, M. A. X. & Wolf, E. *Principles of Optics (Sixth Edition)* (Pergamon, 1980).

19 Coskun, A. & Oosterhuis, W. P. Statistical distributions commonly used in measurement uncertainty in laboratory medicine. *Biochemia Medica* **30** (2020).

20 Tanouchi, Y. *et al.* A noisy linear map underlies oscillations in cell size and gene expression in bacteria. *Nature* **523**, 357-360 (2015).

21 Friedman, H., Lu, P. & Rich, A. Temperature Control of Initiation of Protein Synthesis in Escherichi-Coli. *J. Mol. Biol.* **61**, 105-121 (1971).

22 Broeze, R. J., Solomon, C. J. & Pope, D. H. Effects of low temperature on in vivo and in vitro protein synthesis in Escherichia coli and Pseudomonas fluorescens. *J. Bacteriol.* **134**, 861-874 (1978).

23 Phadtare, S., Inouye, M. & Severinov, K. The nucleic acid melting activity of Escherichia coli CspE is critical for transcription antitermination and cold acclimation of cells. *J. Biol. Chem.* **277**, 7239-7245 (2002).

24 Jones, P. G., Mitta, M., Kim, Y., Jiang, W. & Inouye, M. Cold shock induces a major ribosomal-associated protein that unwinds double-stranded RNA in Escherichia coli. *Proc. Natl. Acad. Sci. U.S.A.* **93**, 76-80 (1996).

25 Horn, G., Hofweber, R., Kremer, W. & Kalbitzer, H. R. Structure and function of bacterial cold shock proteins. *Cell. Mol. Life Sci.* **64**, 1457-1470 (2007).

26 Giuliodori, A. M., Brandi, A., Gualerzi, C. O. & Pon, C. L. Preferential translation of cold-shock mRNAs during cold adaptation. *RNA* **10**, 265-276 (2004).

27 Taheri-Araghi, S. *et al.* Cell-Size Control and Homeostasis in Bacteria. *Curr. Biol.* **25**, 385-391 (2015).

28 Scott, M. & Hwa, T. Shaping bacterial gene expression by physiological and proteome allocation constraints. *Nat. Rev. Microbiol.* **21**, 327-342 (2023).

29 Scott, M., Gunderson, C. W., Mateescu, E. M., Zhang, Z. G. & Hwa, T. Interdependence of Cell Growth and Gene Expression: Origins and Consequences. *Science* **330**, 1099-1102 (2010).

30 Sharma, I. M. & Woodson, S. A. RbfA and IF3 couple ribosome biogenesis and translation initiation to increase stress tolerance. *Nucleic Acids Res.* **48**, 359-372 (2020).

31 Brandi, A. *et al.* Translation initiation factor IF2 contributes to ribosome assembly and maturation during cold adaptation. *Nucleic Acids Res.* **47**, 4652-4662 (2019).

32 Amir, A. Cell Size Regulation in Bacteria. *Phys. Rev. Lett.* **112** (2014).

33 Campos, M. *et al.* A Constant Size Extension Drives Bacterial Cell Size Homeostasis. *Cell* **159**, 1433-1446 (2014).

34 Monod, J. The Growth of Bacterial Cultures. *Annu. Rev. Microbiol.* **3**, 371-394 (1949).

35 Klumpp, S., Zhang, Z. G. & Hwa, T. Growth Rate-Dependent Global Effects on Gene Expression in Bacteria. *Cell* **139**, 1366-1375 (2009).

36 Koch, A. L. Some Calculations on Turbidity of Mitochondria and Bacteria. *Biochim. Biophys. Acta* **51**, 429-441 (1961).

37 Ishimaru, A. *Wave propagation and scattering in random media* (Academic press New York, 1978).

38 Koch, A. L. Turbidity Measurements of Bacterial Cultures in Some Available Commercial Instruments. *Anal. Biochem.* **38**, 252-259 (1970).

39 Bakshi, S. *et al.* Tracking bacterial lineages in complex and dynamic environments with applications for growth control and persistence. *Nat. Microbiol.* **6**, 783-791 (2021).

40 Groen, F. C. A., Young, I. T. & Ligthart, G. A comparison of different focus functions for use in autofocus algorithms. *Cytometry* **6**, 81-91 (1985).

41 Geusebroek, J. M., Cornelissen, F., Smeulders, A. W. M. & Geerts, H. Robust autofocusing in microscopy. *Cytometry* **39**, 1-9 (2000).

42 Zhu, M. L., Mu, H. Y. & Dai, X. F. Integrated control of bacterial growth and stress response by (p)ppGpp in Escherichia coli: A seesaw fashion. *Iscience* **27** (2024).

43 Wallden, M., Fange, D., Lundius, E. G., Baltekin, Ö. & Elf, J. The Synchronization of Replication and Division Cycles in Individual E. coli Cells. *Cell* **166**, 729-739 (2016).

44 Mahone, C. R. & Goley, E. D. Bacterial cell division at a glance. *J. Cell Sci.* **133** (2020).

Methods

Numerical computations of the optical model

Diffraction patterns near the focus of the optical system with circular aperture and coma aberrations can be handled by analyzing the wavefront distortion of an off-axis beam. The objective lens is treated as an ideal lens for the model demonstration. Consider an incident collimated Gaussian beam passing through the lens of radius a and focal length f. The coma aberration function can also be expressed in the polar coordinates (ρ, θ) whose origin is the center of the pupil by $\Phi(\rho, \theta) = A_C\rho^3 \cos\theta$, where A_C is the coefficient of primary coma[45]. Using the Huygens-Fresnel principle, the complex amplitude $U(P)$ is determined by calculating the diffraction integral over the intersection area S on the reference sphere[18]:

$$U(P) = -\frac{\mathrm{i}k}{2\pi}\int\int_S U(Q)\frac{\exp(\mathrm{i}kq)}{q}\mathrm{d}S \tag{3}$$

where k is the wavenumber, and q is the distance between points Q and P. For the incident beam with small off-axis amount involved, the variation of the inclination factor in equation (3) over the integral area can be neglected. The polar coordinates (ρ, θ) are translated to (r, φ) with the origin of which (ρ_0, θ_0) is situated at the beam center for convenience. The amplitude distribution of the Gaussian beam is given by $A_G \exp(-a^2r^2 / \omega^2)$, where A_G is constant amplitude, and ω is beam waist. Furthermore, cylindrical coordinates (u, v, ψ) are introduced to specify an arbitrary point P in the image field where ψ is the azimuth at the focal plane (x, y), the dimensionless coordinates $v = ka\,(x^2 + y^2)^{1/2} / f = k\beta\,(x^2 + y^2)^{1/2}$ and $u = k\beta^2 z$. Then $U(P)$ is given by:

$$U(P) = -\frac{\mathrm{i}kA_G\beta^2}{2\pi}\int_0^{2\pi}\int_0^1 e^{-a^2r^2/\omega^2}e^{\mathrm{i}k\Phi_{TOTAL}(r,\varphi)}\,r\mathrm{d}r\mathrm{d}\varphi \tag{4}$$

The total phase term of Φ_{TOTAL} is defined by combining the like terms:

$$\begin{aligned} k\Phi_{TOTAL}(r,\varphi) &= k\Phi(r,\varphi) + k(q-f) \\ &= L_C + L_0(r) + L_1(r)\cos 2\varphi + L_2(r)\cos\varphi + L_3(r)\cos(\varphi-\psi) \end{aligned} \tag{5}$$

Define $\eta = (L_2^2 + L_3^2 + 2L_2L_3 \cos\psi)^{1/2}$, $\tan\chi = -L_3 \sin\psi / (L_2 + L_3 \cos\psi)$. The integral difficulty of the intensity is simplified by expanding the exponential term $\exp(ik\Phi_{TOTAL})$ with the help of the Jacobi-Anger identity and Graf's addition theorem, substituting the expended series in the integration, and integrating term-wise against φ. The intensity distribution of the diffraction pattern is developed in an infinite series:

$$I(u,v,\psi) = 4k^2 {A_G}^2 \beta^4 \left| e^{\mathrm{i}L_C} \sum_{s=0}^{\infty} (-\mathrm{i})^s \int_0^1 e^{-a^2r^2/\omega^2} e^{\mathrm{i}L_0} J_s(L_1) J_{2s}(\eta) \cos(2s \cdot \chi)\, r\, \mathrm{d}r \right|^2 \quad (6)$$

where J is a Bessel function of first kind. The term $s = 0$ is taken with the factor 1/2. Tedious calculation can be avoided because four terms in this expansion would suffice to keep the intensity variation within a few percent. The simplification greatly speeds up the numerical calculation of the intensity distribution (Supplementary Note 2). In the numerical computation, the selection of each parameter is as close to the actual optical path configuration as possible, such as $\beta = 1.25$ for the 100× objective lens, relative beam position ($\rho_0 = 0.1$, $\theta_0 = 0°$), and coma coefficient $A_C = 16\pi / k$. The coefficient A_C is proportional to the tilt angle of the beam incident on the objective, and we have chosen a more representative value here.

Optical setup of the microscope and LUNA

The optomechanical design was performed using CAD software (Dassault Systemes, SolidWorks). An infinity microscope based on a commercialized microscope frame (Applied Scientific Instrumentation, RAMM) and a set of precision machined components was custom-built. The specimen was mounted on a motorized stage (MS2000) for planar motion. Axial movement of the objective was achieved by a motorized actuator with a step resolution of 22 nm (LS50). Kohler illumination with a neutral white light source (Thorlabs, MNWHL4) was designed to provide brightfield and phase-contrast imaging mode. High-resolution images were collected using a sCMOS camera (PCO, Panda 4.2) with a 6.5 μm pixel size.

LUNA was installed in this microscope system. The light source was a fiber-coupled laser with a wavelength of 650 nm (output power < 5 mw), and was collimated to parallel beam by a fiber collimator. The wavelength was chosen to avoid crosstalk with the illumination for our bacteria imaging experiments and for a lower cost, although an infrared wavelength for more general applications could also be selected.

An aspheric lens was inserted as the focal length extender (FLE), shifting the focal point of the laser beam to optimize the focusing range. The off-axis laser beam was introduced into the microscope optical train by a shortpass dichroic mirror (Semrock, FF625-SDi01). The diffraction pattern at the reflection plane was projected on a detector (Thorlabs, DCC1545M), whose pixel size is 5.2 μm. A cylindrical lens was placed before the detector to shape the diffraction pattern one-dimensionally to improve the detection accuracy. The full width at half maximum of the line projection of the crescent spot was approximately 30 μm wide, ensuring adequate subpixel accuracy. During the autofocusing procedure, a practical proportional-integral controller was used. Although LUNA was implemented on a bespoke microscope system, it is also compatible with other commercial microscopes with infinity optics. Four objective lenses were tested for LUNA's performance (Extended Data Table 1). Unless otherwise stated, data presented in the text was collected from the 100× objective.

Ray tracing simulation

The optical design and numerical simulation of LUNA's optics were carried out based on ray tracing software (Zemax, OpticStudio). A set of lenses was used to combine to substitute objective with an equivalent magnification of 100×. The other parameters of the optical elements were set exactly the same as the optical setup. For off-axis incidence, the normalized radial coordinate of the beam center at the objective rear aperture was specified to be approximately 0.15 (Extended Data Fig. 1c). A reflection surface was placed at the imaging space of the objective. Sequential intensity distributions on the reflection and detection plane were recorded as the reflection surface changes along the optical axis.

Calibration of defocus dependence

The measurement was carried out by scanning the objective from bottom to top along the optical axis around the focal plane. The reflected images on the detector were repeatedly recorded five times in repetitions at each step. An anti-backlash routine was introduced at each step to advantage for precision movement. The centroid coordinates of the light spot at sub-pixel precision were then computed from the captured images through basic morphological processing. The linear range was determined by finding the

494 maximum *N* multiples of DOF while maintaining the fitting root mean squared error (*RMSE*) less than 1
495 (Extended Data Fig. 2c). The strict criteria for the linear range determination were selected to obtain high
496 focusing sensitivity and accuracy near the focal plane.

497 Measurement repeatability is defined as the proportion of the total variation accounted for by the
498 system variation to assess the system's measurement variation[46]. It indicates the degree of consistency
499 during multiple measurements. The pooled standard deviation was used to calculate this variation
500 underlying the monotonic response curve. A ratio below 10% is indicative of satisfactory system
501 performance[47].

502 **Performance test of LUNA**

503 Timelapse tests with specific time intervals (1 second) were carried out and lasted for one hour for the
504 four objectives. Discrete drift thresholds varying from 5 nm to 50 nm at intervals of 5 nm were tested in
505 each condition. For the tests evaluating the focusing time, the time interval was altered. The objective and
506 sample temperature were maintained at 37 °C.

507 The extent of the perturbations can be reflected in the temporal fluctuations of spot intensity on the
508 same focal plane. This fluctuation may originate from laser instability, thermal effects in optical elements,
509 etc. The distribution parameters were extracted from the detector images. Random Gaussian noise
510 conforming to this distribution was generated and superimposed onto different spot images to simulate the
511 fluctuations, and the simulation was repeated 100 times on each image. Errors of the centroid locations
512 were employed to evaluate the impact of perturbations.

513 **Single-cell culture on microfluidic device**

514 A microfluidic chip was employed to track the long-term growth of bacteria, the structure of which
515 follows that of previously published: it consists of a series of microchannels perpendicular to the main
516 trench that perfuse the fresh medium[48]. The chip was fabricated based on soft lithography technique by
517 mixing dimethylsiloxane monomer and curing agent (Dow Corning, SYLGARD 184 Silicone Elastomer

518 Kit) in a ratio of 10:1, and then pouring into a mould, degassing and curing at 80 °C for one hour. The
519 PDMS chip was punched and bonded to a clean coverslip by air plasma treatment (Harrick Plasma, PDC-
520 002) for 30 seconds, followed by baking at 80 °C for five minutes. The microfluidic chip was fixed into a
521 custom-designed water bath incubator, which adapts to the microscope stage (Extended Data Fig. 3b). The
522 incubator can be filled with distilled water in which the microfluidic chip is submerged. Rubber rings are
523 used in the design of the incubator to prevent water seepage. The sealable incubator has two pairs of fluidic
524 conduits: fresh medium flows through the chip for cell growth; distilled water is circulated into the
525 incubator for temperature change and maintenance.

526 *E. coli* K12 strains MC4100 and MG1655 were measured (MC4100 is presented in the text), in which
527 the flagella structural protein gene *fliC* and fimbriae structural protein gene *fimA* of MG1655 were knocked
528 out to prevent their escape from the microchannels. EZ rich defined medium (RDM) supplement with 0.4%
529 glucose was used[49]. The overnight culture grown from several colonies was subcultured twice and
530 centrifuged at a sufficiently high density. The concentrated culture was injected into the cleaned chip
531 passivated with bovine serum albumin, and the chip was spun to load cells into the microchannels. Fresh
532 medium was infused into the chip at a rate of 500 μL/hr by a pressure controller (FluidicLab, PC1) equipped
533 with a 0.22 μm filter. Next, the incubator with the chip was sealed and placed on the microscope stage for
534 time-lapse imaging.

535 **Time-lapse imaging of bacterial under CS**

536 We developed a control software using MATLAB for the time-lapse imaging in the bespoke
537 microscope. Users could set up imaging conditions and perform automation of experiments. The
538 autofocusing control is integrated, with the user only needing to set the desired plane as the focal plane.
539 The output laser power of LUNA at the objective front aperture was adjusted to ~5 μw, and the threshold
540 was set as 50 nm.

541 Phase-contrast images were acquired with the 100× objective. Multiple microchannel sites (around 45
542 in each repeat experiment) were imaged every minute for 24-30 hours. Each image acquisition started right

543 after an autofocusing procedure. Approximately 1,100 single-cell data in total were collected in each repeat.
544 The culture temperature was maintained by the circulation of distilled water in an external thermostatic
545 water bath driven by a peristaltic pump. Cells were cultured at 37 °C to steady-state for about four hours
546 before CS. By mixing ice into the external water bath, the incubator temperature can be downshifted to
547 14 °C within 5 minutes and maintained until the end of the time-lapse experiment. When the temperature
548 was lowered, the objective lens heater was stopped, which caused a slightly longer focusing time. At least
549 3 repeated experiments were carried out for each of the two strains.

550 **Image analysis and data process**

551 Hundreds of cells at the bottom of microchannels were imaged sequentially. We developed a custom
552 algorithm routine to analyze phase-contrast images using MATLAB: Microfluidic Architecture based
553 Resilient Contour Expansion Analysis (MARCEA) (Extended Data Fig. 3c). Raw images were denoised
554 and segmented to identify individual cells. The contours of the segmented cells were iteratively adjusted
555 based on a rod-shaped model to adapt to the deformation of the cells, thereby extracting their accurate
556 spatial features. Microchannels were automatically aligned for cell tracking (Extended Data Fig. 3d). A
557 cell division event was determined according to the large drop of the width and intensity at the split position.
558 Using the processing routine, complete analysis of ~65,000 images costs ~80 mins for each experiment on
559 a standard computer with ten physical cores.

560 A total of 10,040 cell cycles from 784 lineages were used to statistically analyze their behaviors.
561 Outliers within each cell cycle were ignored when calculating those time-dependent properties including
562 sizes and elongation rates. Aberrant cell cycles such as filamentation were excluded from each experiment.
563 Groupings of cell lineages according to their relative moments (values from 0 to 1) of CS onset within G0
564 lifespan were employed. Groupings are centered at intervals of 0.1, and each group encompasses a range
565 of ± 0.05 around the center value.

566 **Experiments of batch culture**

567 Both *E. coli* MC4100 and MG1655 strains were measured (MC4100 is presented in the text unless
568 otherwise stated). A few single colonies from a Luria-Bertani agar plate were picked. Cells were cultured
569 overnight at 37 °C in RDM and then placed in a thermostatic shaking water bath at 37 °C after subculture
570 three times (> 10 mass doublings). The bacterial population was proven to reach a steady-state by then[49].
571 The measurements started when the cells were diluted again to an OD of 0.02 at 600 nm, with a sampling
572 interval of 15-30 minutes. The OD_{600} value was determined using a spectrophotometer (Thermo Fisher
573 Scientific, Genesys 150), with an average of three readings taken. 50 µl of the cell suspension was taken
574 and fixed with the 450 µl of precooled fixation buffer (0.12% formaldehyde with 0.9% NaCl, filtered with
575 a 0.22 µm filter), then used to measure the cell concentration and volume through a flow cytometer
576 (Beckman Coulter, CytoFLEX S) in three parallel samples (Supplementary Note 5). Average cell volume
577 was determined by the median of the forward scatter signals (FSC-A). A variant method called axial light
578 loss detection is employed on the cytometer to detect FSC intensity, which is directly proportional to the
579 cell volume regardless of the refractive index and thus benefits[50]. Further quantitative research also
580 supports the relationship[49]. For the experiments with CS, when OD_{600} reached about 0.2, the culture
581 temperature was gradually lowered to 14 °C or 12 °C within five minutes by mixing ice into the water bath.

582 **Total protein quantification**

583 Total protein quantification was carried out according to previous studies using the Biuret method[51,52].
584 We quantified changes in total protein to represent ΔM since M is roughly proportional to the protein
585 amount[53]. The MG1655 strain was selected and followed the culture procedure. The temperature was
586 lowered to 12 °C to ensure a sufficiently long acclimation (~5 hours) and higher resolution. Two sampling
587 time points were at the beginning and near the end of the acclimation, respectively. Cell cultures were
588 collected by centrifugation in triplicate (4 ml each) at each time point. The cell pellet was rinsed with 1 ml
589 0.9% NaCl solution, re-suspended in 0.2 ml water, and snap frozen in liquid nitrogen. The cell pellet was
590 then thawed in a room temperature (RT) water bath. To extract proteins, 0.1 ml 3M NaOH was added,
591 incubated at 100 °C heat block for 5 min, and cooled in water bath at RT for 5 min. Then 0.1 ml 1.6%

$CuSO_4$ was added to the sample, shaken and mixed thoroughly, and allowed to stand for 5 min. The sample was centrifuged and OD value at 555 nm was read by the spectrophotometer. The protein amount of the sample was determined from the standard curve of bovine serum albumin obtained on the day of the experiment using the same procedure.

Simulation with the Rayleigh-Gans approximation

The intraparticle interference can be corrected by introducing a form function $P(\theta)$ to the Rayleigh differential scattering cross section σ_d. If the relative refractive index of the scatterer in the surrounding medium ($m = n_s / n_m$) approaches to 1, σ_d can be simplified as:

$$\sigma_d = \frac{\mathrm{d}\sigma}{\mathrm{d}\Omega} = \frac{k'^4 V^2}{8\pi^2}(m-1)^2(1+\cos^2\theta)P(\theta) \tag{7}$$

where k' is the wavenumber in the medium, V is scatterer's volume, and θ is angle of observation. The refractive indices of *E. coli* and the surrounding medium are estimated as 1.384 and 1.338 at illumination wavelength of 600 nm[54], respectively, thus meeting the prerequisites of the above equation. Furthermore, the refractive index difference between the scatterer and the medium is proportional to the dry-mass density ρ_{dry}, with a scaling factor of the specific refraction index increment[54-56], hence the quantity (m – 1) can be substituted by ρ_{dry}. The $P(\theta)$ for differently shaped scatterers have different analytical forms. Ellipsoid of revolution as the form function is adopted to describe single *E. coli* cell, which has the following form:

$$P = \left[\frac{3}{x^3}(\sin x - x\cos x)\right]^2, x = k'w\sin\frac{\theta}{2}\sqrt{\sin^2\beta + \gamma^2\cos^2\beta} \tag{8}$$

where β is the orientation angle between the ellipsoid and the direction bisecting the incident and the scattered light beam, w is width, and γ is aspect ratio. For randomly oriented bacteria in the medium, the form function should be averaged over all equally probable orientation angle β. Over a thousand cells with appropriate parameter ranges, were simulated to compute the total scattering cross section σ by integrating σ_d over all angles except the detecting regime. Equivalent volume and aspect ratio were chosen as two independent determining parameters (ranging from 0.5 ~ 5 μm^3 and 2.5 ~ 5, respectively) to simulate cells.

To account for the uncertainty in the detection angle, we combined a series of integrals with lower bounds on θ varying from 0.5° to 3° at 0.5° interval and upper bounds of 180°.

Data availability

All the data used in this study are available upon reasonable request to the corresponding author.

Code availability

All codes are available upon reasonable request to the corresponding author for nonprofit academic research use only. Codes for controlling the LUNA-enabled bespoke microscope and analyzing raw images are available in executable forms.

References

45 Yoshida, A. & Asakura, T. Diffraction Patterns of Off-Axis Gaussian Beams in Optical System with Astigmatism and Coma. *Opt. Commun.* **25**, 133-136 (1978).

46 Nakagawa, S. & Schielzeth, H. Repeatability for Gaussian and non-Gaussian data: a practical guide for biologists. *Biol. Rev.* **85**, 935-956 (2010).

47 Chrysler Corporation, F. M. C., General Motors Corporation. *Measurement Systems Analysis (MSA)* (AIAG, 2010).

48 Wang, P. *et al.* Robust Growth of Escherichia coli. *Curr. Biol.* **20**, 1099-1103 (2010).

49 Zheng, H. *et al.* General quantitative relations linking cell growth and the cell cycle in. *Nat. Microbiol.* **5**, 995-1001 (2020).

50 Brittain, G. I. V. *et al.* A Novel Semiconductor-Based Flow Cytometer with Enhanced Light-Scatter Sensitivity for the Analysis of Biological Nanoparticles. *Sci. Rep.* **9** (2019).

51 You, C. H. *et al.* Coordination of bacterial proteome with metabolism by cyclic AMP signalling. *Nature* **500**, 301-306 (2013).

52 Herbert, D., Phipps, P. & Strange, R. *Methods in microbiology* (Elsevier, 1971).

53 Basan, M. *et al.* Inflating bacterial cells by increased protein synthesis. *Mol. Syst. Biol.* **11** (2015).

54 Oldewurtel, E. R., Kitahara, Y. & van Teeffelen, S. Robust surface-to-mass coupling and turgor-dependent cell width determine bacterial dry-mass density. *Proc. Natl. Acad. Sci. U.S.A.* **118** (2021).

55 Barer, R. Interference Microscopy and Mass Determination. *Nature* **169**, 366-367 (1952).

56 Koch, A. L., Robertson, B. R. & Button, D. K. Deduction of the cell volume and mass from forward scatter intensity of bacteria analyzed by flow cytometry. *J. Microbiol. Methods* **27**, 49-61 (1996).

Acknowledgements

We thank H. Cao for providing MG1655 strain. We thank H. Zheng for discussions. This work was supported by the National Key R&D Program of China (Grant No. 2020YFA0908800), Strategic Priority Research Program of the Chinese Academy of Sciences (Grant No. XDB0480000), National Natural Science Foundation of China (Grant No. 32071417).

Author contributions

S.L. devised LUNA, developed the optical model and numerical simulation, performed the implementation and evaluation of LUNA, devised and implemented the LUNA-enabled bespoke microscope system, developed the standalone control software, developed image processing algorithm MARCEA, developed the scattering model and performed simulations on OD measurements, and analyzed all the experiments data. Z.M. participated in the evaluation of LUNA, conceived the biological experiments, prepared the bacteria samples, performed the biological experiments, and participated in the biological data analysis. Y.Y. designed the microfluidic chip, conceived the biological experiments, and participated in the biological data analysis. J.W. and Y.S. prepared the bacteria samples and performed the biological experiments. X.C. participated in the discussion of optical principle and the evaluation of LUNA. X.F. participated in the discussion of biological experiments. S.H. conceived the whole project and supervised the research. S.L. wrote the paper with contributions from all of the authors.

Competing interests

The authors declare no competing interests.

Supplementary Information is available for this paper.

Correspondence and requests for materials should be addressed to Shuqiang HUANG.

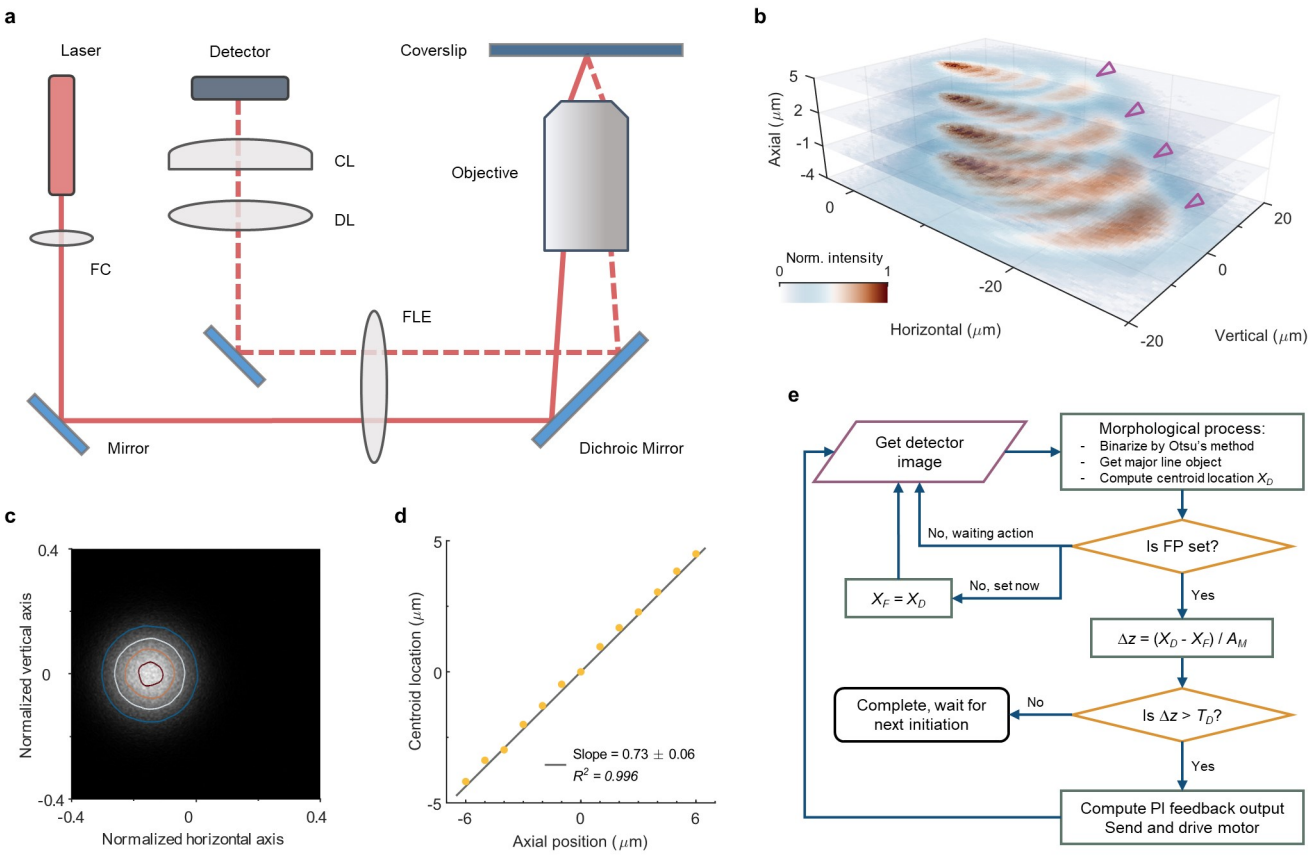

Extended Data Fig. 1 | Implementation of LUNA. a, Schematic of optical path. The laser beam was reflected into the bespoke microscope by a dichroic mirror. Dashed line: reflected light. FC, fiber collimator; CL, cylindrical lens; DL, detector lens; FLE, focal length extender. The implementation of LUNA in microscope follows this design. **b**, Intensities on the reflection planes in the ray tracing simulation. Images at each axial position were individually normalized. Triangle markers indicate the outermost crescent spots. **c**, Intensity on the entrance pupil plane in the simulation. Polar coordinates were normalized by the aperture of the objective. Colored lines indicate isophotes. Beam center distance is approximately $\rho_0 = 0.15$. **d**, Magnified defocus distance on the reflection plane in the simulation. Linear regression with slope (95% confidence intervals) and fit goodness is shown. **e**, Flowchart of LUNA. FP, focal plane; A_M, effective magnification from axial position to centroid location; X_F, focal plane location; Δz, detected drift; T_D, set threshold; PI, proportional-integral controller. Morphological process costs ~2 ms on the control computer with 3.60 GHz CPU.

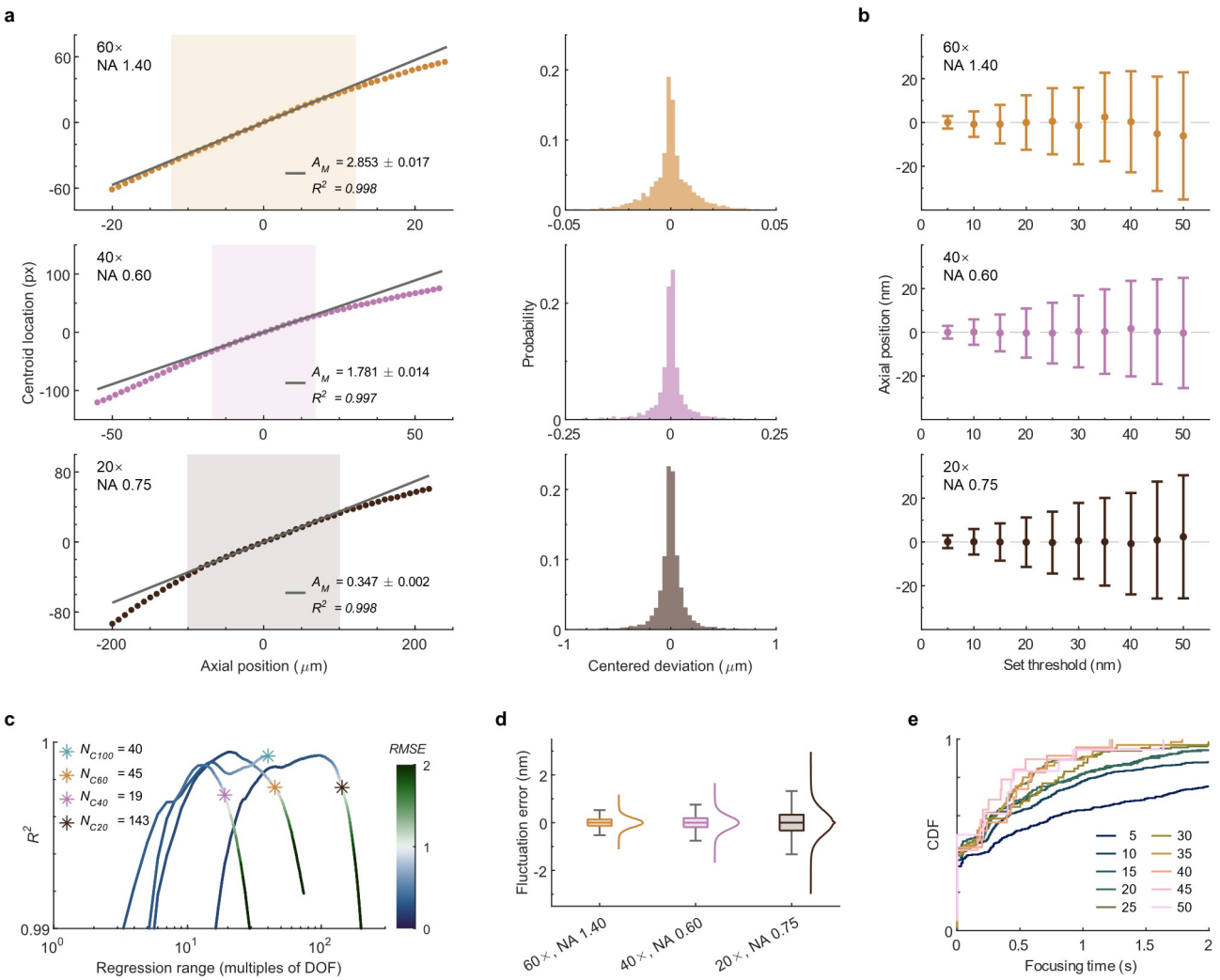

Extended Data Fig. 2 | Supplemental performance metrics of LUNA. a, Calibration curve (left) and measurement error distribution (right) for representative objectives. Shaded regions in the left panels indicate the linear range of the corresponding objective. Linear regressions with slope (95% confidence intervals) and fit goodness are shown. **b**, Focusing accuracy and precision assessment. Dots and error bars represent the mean and s.d. values of the focus errors. **c**, Evaluation metrics of linear regressions under different range. The regression range was symmetrically selected with the zero point as the center and multiples of the corresponding DOF. Critical *N* multiples of DOF was determined by restricting the fitting *RMSE* less than 1. **d**, Impacts of laser fluctuations on focusing accuracy. Grouped data are presented as box plots with the edges at the 0.25 and 0.75 quantiles, the central line at the median, and the whiskers at the minima and maxima within 1.5× interquartile range from the box. Colored lines, probability distributions. **e**, Cumulative distribution function of focusing time at 1 Hz measurement. Colored lines indicate different set thresholds, unit in nm.

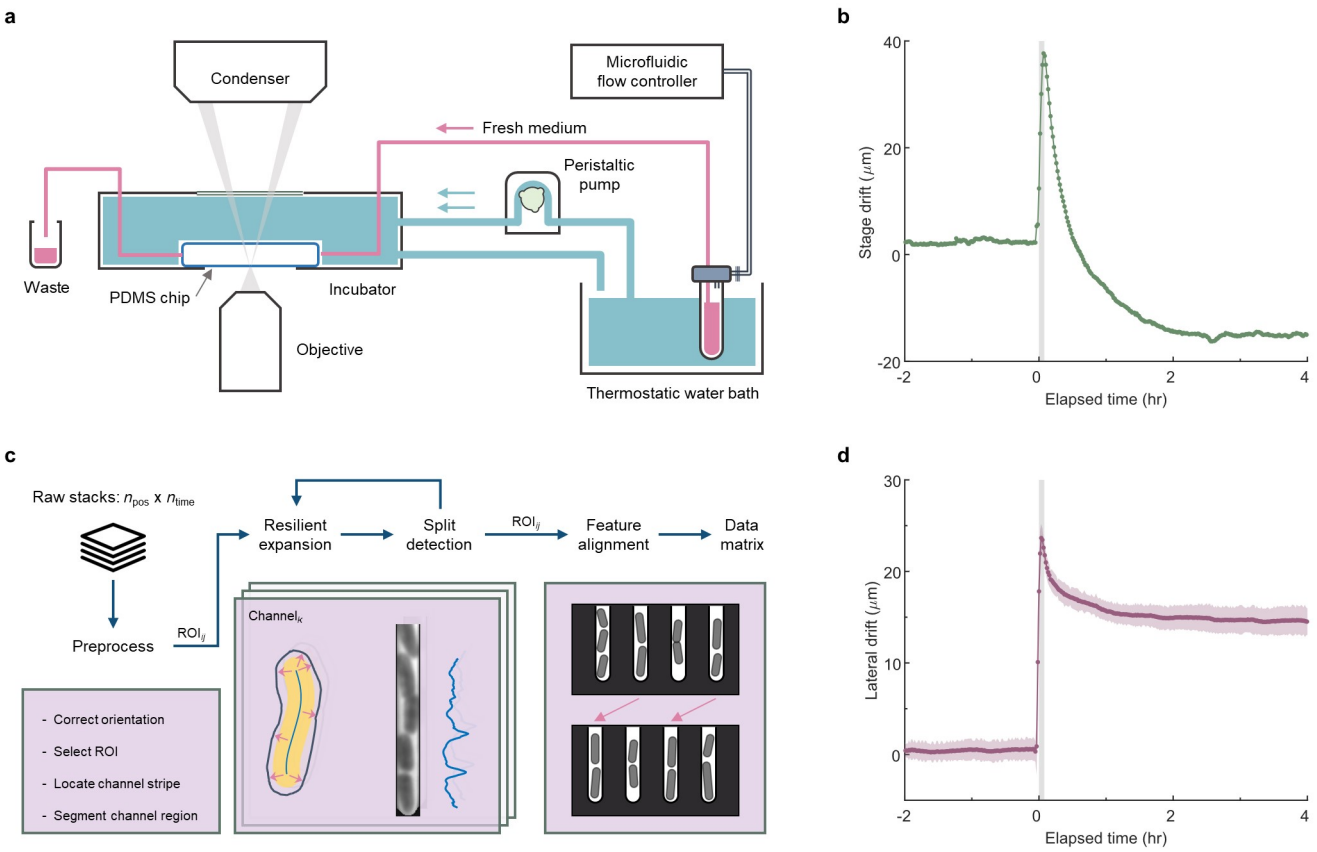

Extended Data Fig. 3 | Monitoring the physiological dynamics of bacterial cells during CS. a, Schematic of our microfluidic-based temperature control device. **b**, Stage drift over time. **c**, Microfluidic Architecture based Resilient Contour Expansion Analysis (MARCEA) pipeline. ROI, region of interest. **d**, Lateral drift of imaging sites over time. In **b** and **d**, data in scatter form represent the average of all imaged sites (n = 45). Shaded region indicates the rapid temperature drop period. Error bands, s.e.m.

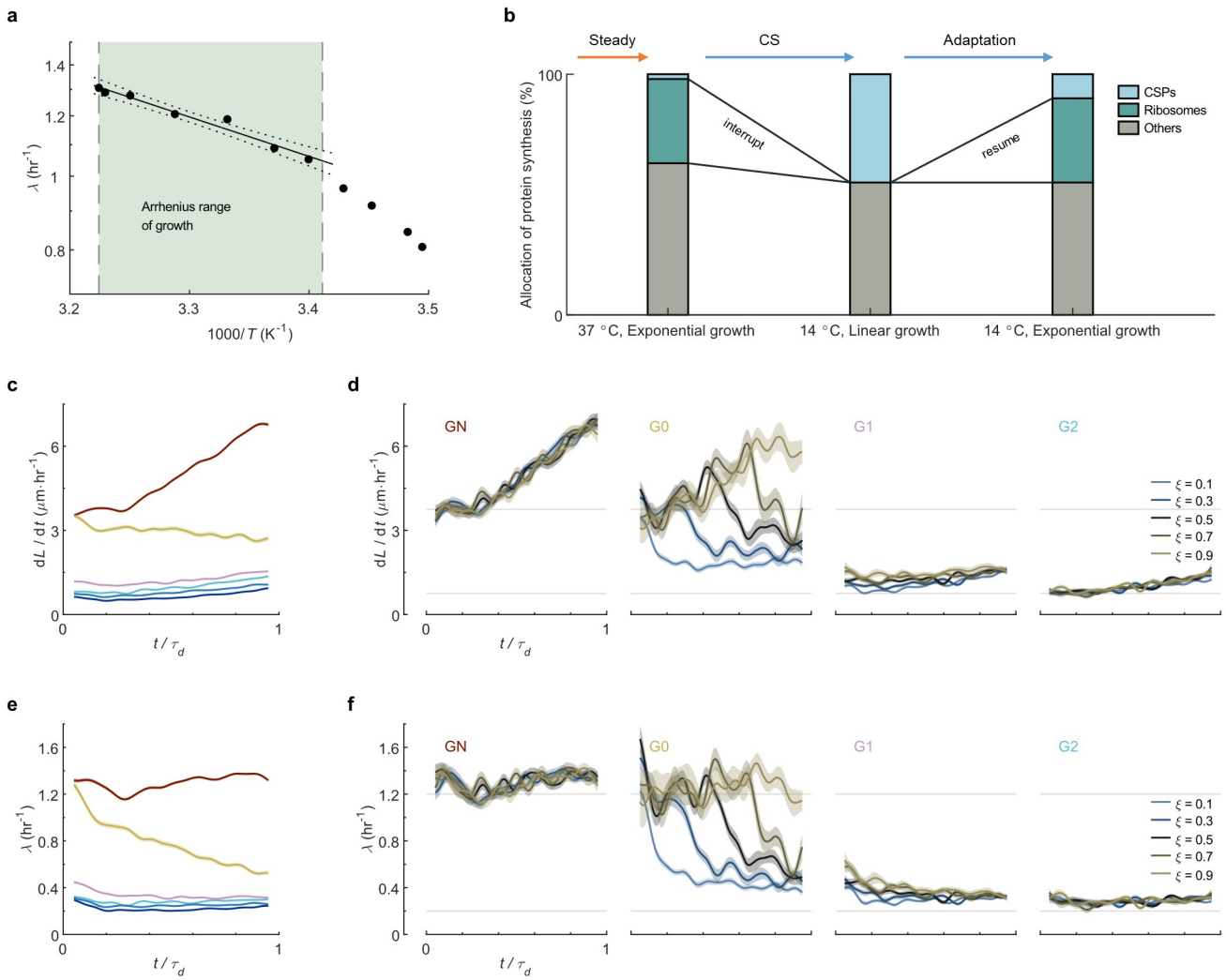

Extended Data Fig. 4 | Supplemental single-cell growth dynamics and analysis at sub-cell-cycle resolution. a, Temperature dependence of growth rate during the dynamic cooling process. Linear fitting to the reciprocal temperature and logarithm of λ is shown as line. Dot lines indicate the 95% prediction bounds. Arrhenius range of growth is shaded. **b**, A rough illustration of the allocation of different proteins synthesis at different stage during CSR. Percentage data were retrieved from reference[1,15,29]. **c**, Average elongation rate across generations as function of normalized interdivision time. **d**, Elongation rate details of distinct ξ across generations. **e**, Average growth rate across generations as function of normalized interdivision time. **f**, Growth rate details of distinct ξ across generations. Error bands in **c-f**, s.e.m. The color code in **c** and **e** marks the same generation as in Fig. 3a.

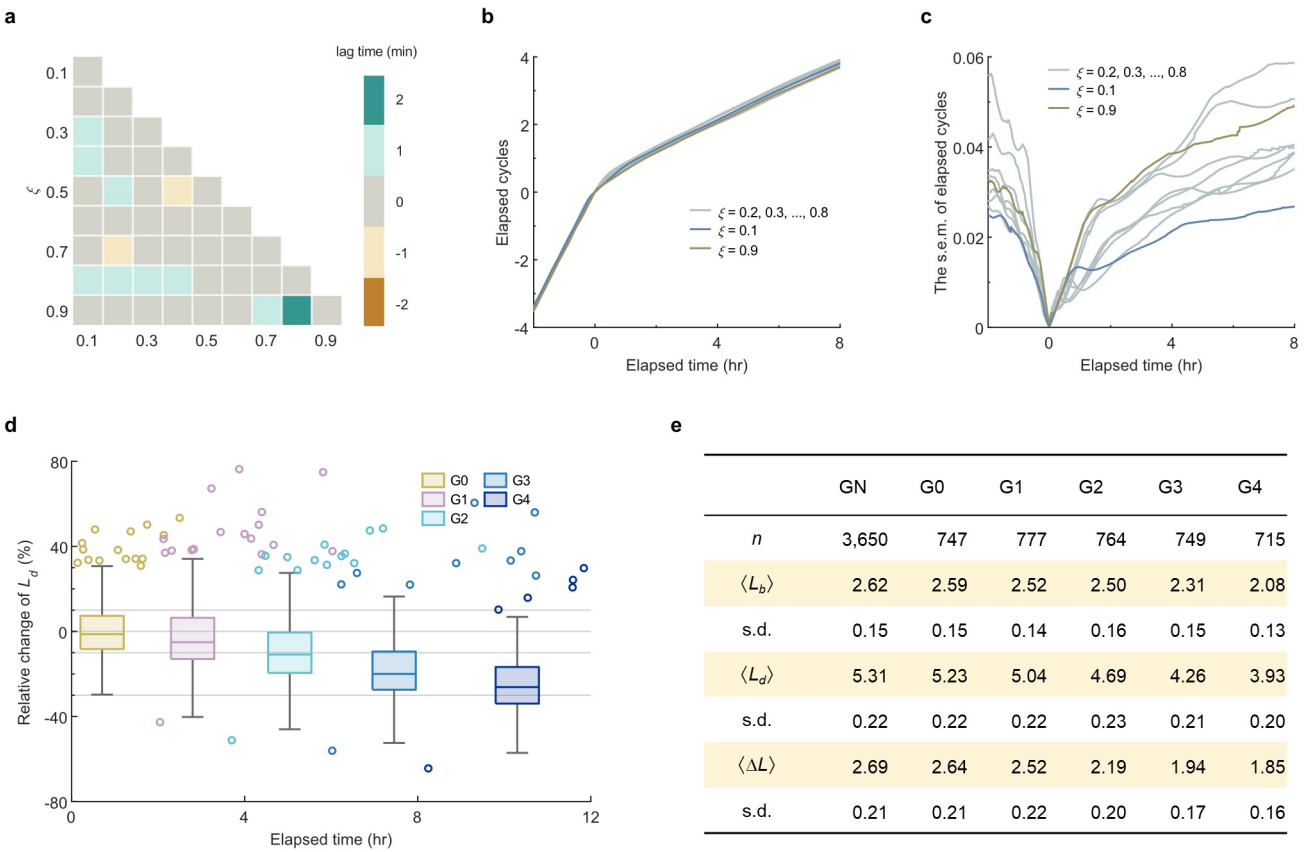

e

	GN	G0	G1	G2	G3	G4
n	3,650	747	777	764	749	715
$\langle L_b \rangle$	2.62	2.59	2.52	2.50	2.31	2.08
s.d.	0.15	0.15	0.14	0.16	0.15	0.13
$\langle L_d \rangle$	5.31	5.23	5.04	4.69	4.26	3.93
s.d.	0.22	0.22	0.22	0.23	0.21	0.20
$\langle \Delta L \rangle$	2.69	2.64	2.52	2.19	1.94	1.85
s.d.	0.21	0.21	0.22	0.20	0.17	0.16

Extended Data Fig. 5 | Supplemental synchronization and length in single-cell phenotypic dynamics. **a**, Lag matrix for distinct groups of ξ. Values were computed by locating the cross-correlation maximum. **b**, Elapsed cycle numbers of all lineages as functions of time. **c**, Errors (s.e.m.) of elapsed cycle numbers as functions of time. Each group is centered by the average. **d**, Percentage change of division length of each generation after CS compares to GN. Data are presented as box plots with the edges at the 0.25 and 0.75 quantiles, the central line at the median, and the whiskers at the minima and maxima within 1.5× interquartile range from the box. Each box is located at the average division time of that generation. Circles, outliers outside the whiskers. **e**, Length data of each generation. Expectation and standard deviation (s.d.) values were computed from the properties of the log-normal distribution of L. Unit in μm, n is the number of cells.

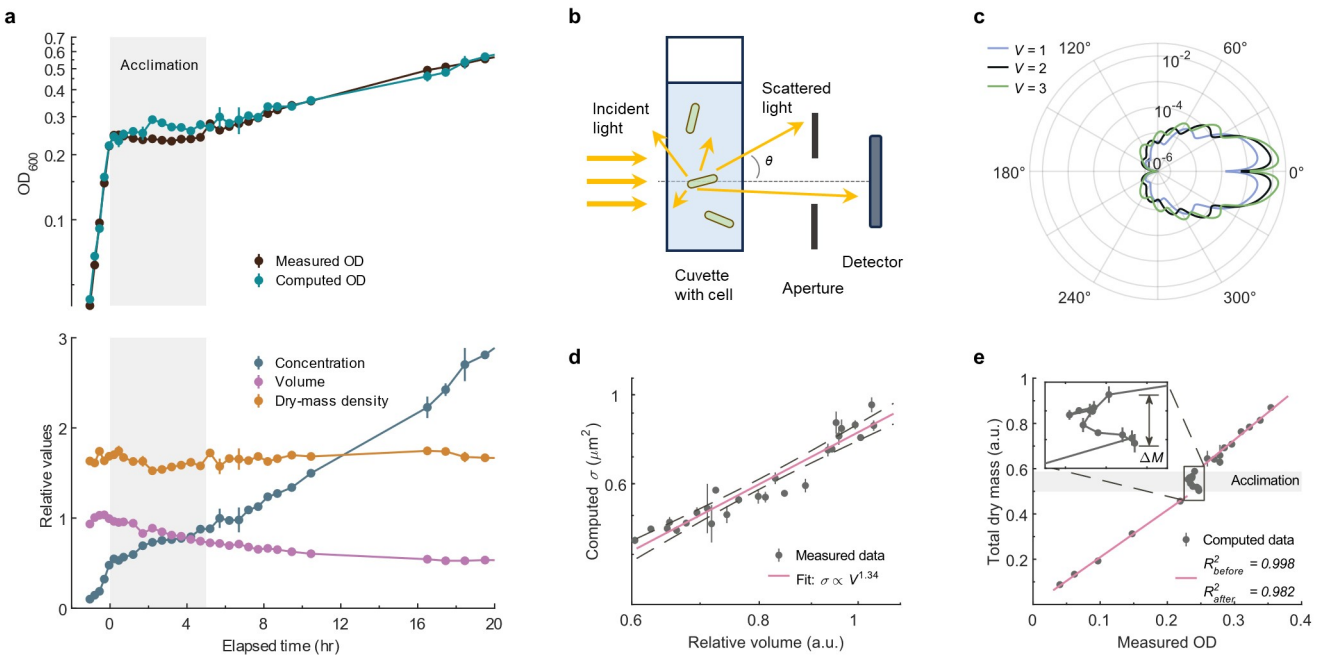

Extended Data Fig. 6 | Supplemental results of batch culture. a, Measurements with temperature dropped to 12 °C. Measured and computed OD_{600} values (top). Computed data was scaled at *t0*. Bottom: cell concentrations and average volumes extracted from the flow cytometer, normalized to *t0* and average value before CS, respectively. Relative cell density was computed and scaled for comparison. Shaded region indicates the acclimation. **b**, Illustration of light scattering by a cell in the suspending medium. A small portion of scattered light is collected by the detector. **c**, Relative angular scattering intensity of single bacteria computed through the numerical simulation. V, equivalent volume in μm^3. **d**, Computed σ from experimental data as function of relative volume. Power exponent was determined by linear regression on the logarithmically transformed data ($R^2 = 0.913$, confidence interval is ±0.17). Dashed lines indicate the 95% prediction bounds. a.u., arbitrary units. **e**, Computed total dry mass plotted as a function of OD, together with linear fittings. Fitting for the acclimation has a R^2 of -0.741 (Pearson correlation coefficient -0.59). Mass increment during the acclimation is indicated as the height of the shaded area and marked in the inset. Error bars in **a**, **d-e**, s.d.

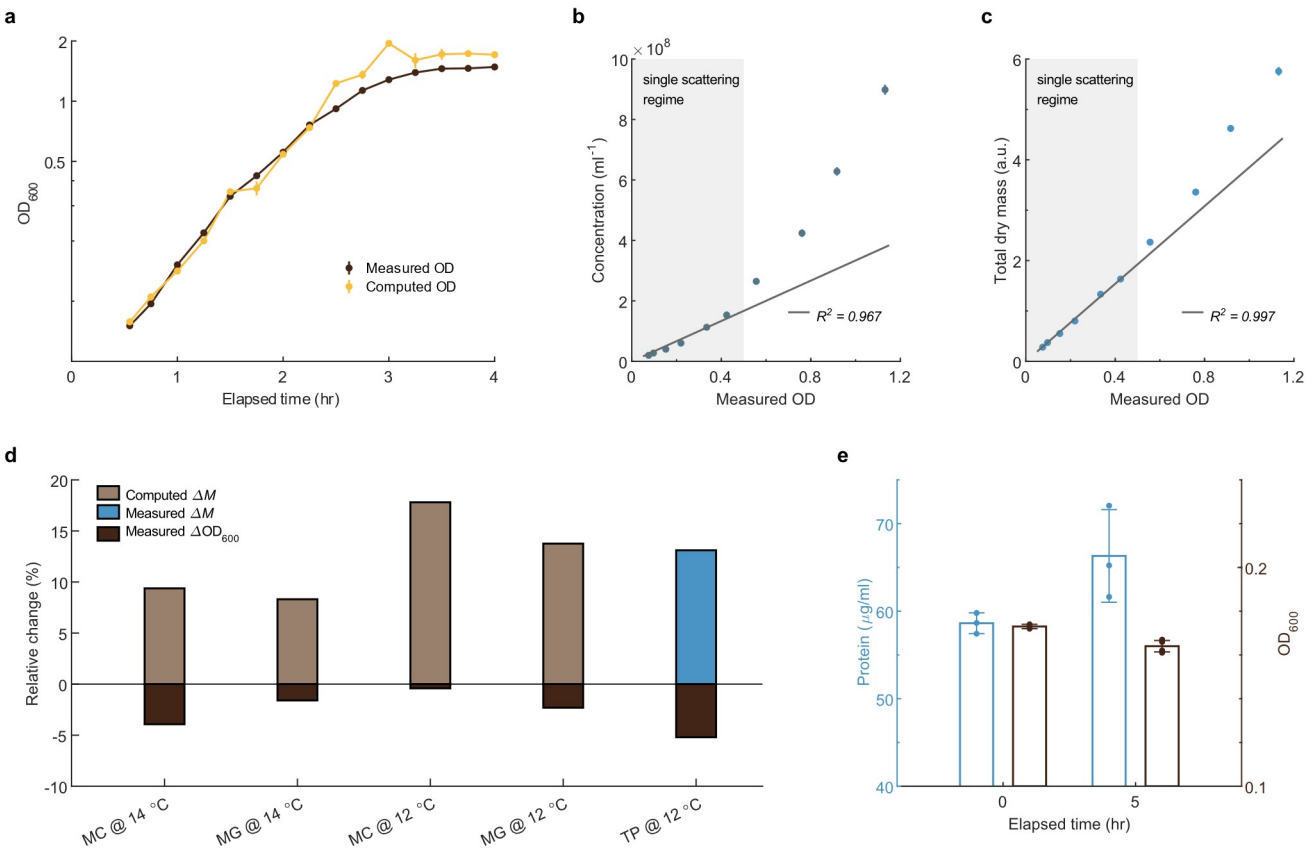

Extended Data Fig. 7 | Supplemental results of batch culture and protein quantification. a, Measured and computed OD_{600} in the batch culture without changing temperature. **b**, **c**, Correlation of measured OD_{600} in **a** with cell concentration and computed dry mass. Linear fittings were performed by data points within shaded area of which OD < 0.5. R^2 of the fitting is shown. **d**, Percentage change of dry mass and OD_{600} during the acclimation. Temperature drops to 12 °C and 14 °C were performed separately for both strains: MC, MC4100 strain; MG, MG1655 strain. TP, total protein of MG1655 strain. **e**, Total protein measurement of the last group in **d**. Error bars in **a-c**, **e**, s.d.

750 **Extended Data Table 1 | LUNA performance results with different objective lenses from Nikon.**

Objective model	Plan Apo λ DM	Plan Apo λ DM	S Plan Fluor ELWD	Super Fluor
Immersion medium	oil	oil	air	air
Magnification (Mag)	100×	60×	40×	20×
Numerical Aperture (NA)	1.45	1.40	0.60	0.75
DOF (μm)	0.46	0.54	1.80	1.41
Focusing range (μm)	18.6	40.1	111.5	400.8
Linear range (μm)	18.6	24.4	34.2	201.8
Measurement repeatability (%)	1.2	1.5	1.7	1.1
Precision (nm)	3.0	2.9	2.9	2.9
Normalized precision (%)	1.3	1.1	0.3	0.4

751 The DOF of the microscope was calculated using the formula DOF = $n \cdot \lambda$ / NA^2 + $n \cdot s$ / Mag / NA. The
752 refractive index n = 1 for the dry objectives, and n = 1.515 for the oil immersion objectives. Wavelength
753 of illumination light λ = 550 nm. Pixel size of the imaging camera s = 6.5 μm. Note that actual focusing
754 range can be slightly larger than the values shown. Precision was calculated at a threshold set as 5 nm.
755 Normalized precision was calculated as twice the ratio of Precision to DOF.